

High thermoelectric power factor in ambient-stable semiconducting rare-earth ErN thin films

Cite as: Appl. Phys. Lett. **118**, 132103 (2021); <https://doi.org/10.1063/5.0041879>

Submitted: 26 December 2020 . Accepted: 16 March 2021 . Published Online: 30 March 2021

 Krithika Upadhyaya,  Vijay Bhatia,  Ashalatha Indiradevi Kamalasanan Pillai,  Magnus Garbrecht, and  Bivas Saha



View Online



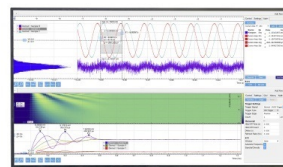
Export Citation



CrossMark

Challenge us.

What are your needs for periodic signal detection?



Zurich Instruments

High thermoelectric power factor in ambient-stable semiconducting rare-earth ErN thin films

Cite as: Appl. Phys. Lett. **118**, 132103 (2021); doi: [10.1063/5.0041879](https://doi.org/10.1063/5.0041879)

Submitted: 26 December 2020 · Accepted: 16 March 2021 ·

Published Online: 30 March 2021



View Online



Export Citation



CrossMark

Krithika Upadhy,^{1,2}  Vijay Bhatia,³  Ashalatha Indiradevi Kamalasanan Pillai,³  Magnus Garbrecht,³  and Bivas Saha^{1,2,4,a)} 

AFFILIATIONS

¹Chemistry and Physics of Materials Unit, Jawaharlal Nehru Centre for Advanced Scientific Research, Bangalore 560064, India

²International Centre for Materials Science, Jawaharlal Nehru Centre for Advanced Scientific Research, Bangalore 560064, India

³Australian Centre for Microscopy and Microanalysis, The University of Sydney, Camperdown, New South Wales 2006, Australia

⁴School of Advanced Materials (SAMat), Jawaharlal Nehru Centre for Advanced Scientific Research, Bangalore 560064, India

^{a)}Author to whom correspondence should be addressed: bsaha@jncasr.ac.in and bivas.mat@gmail.com

ABSTRACT

Erbium nitride (ErN) is an emerging semiconducting rare-earth pnictide with unique electronic and magnetic properties. ErN has attracted significant interest for spin superlattices and spintronic devices and as a second-stage regenerator for Gifford–McMahon cryo-coolers. Solid-solution alloys of ErN with III-nitride semiconductors such as GaN have been studied extensively for use in solid-state lasers, amplifiers, and light-emitting devices operating in the retina-safe and fiber-optic communication wavelength window of 1.54 μm . However, due to the high affinity of Er toward oxygen, ErN is prone to oxidation in ambient conditions. To date, no reports on the deposition of the high-quality ErN thin film and its thermoelectric properties have been published. In this Letter, semiconducting ErN thin films are deposited inside an ultrahigh-vacuum chamber and capped with thin (3 nm) AlN layers to stabilize it in ambient conditions. Structural, optical, and electronic characterization reveals that ErN thin films (a) grow with (111) and (002) orientations on (0001) Al_2O_3 and (001) MgO substrates with sharp and abrupt ErN–substrate interfaces, (b) demonstrate a direct bandgap of 1.9 eV, and (c) exhibit a high carrier concentration in the range of 4.3×10^{20} to $1.4 \times 10^{21} \text{ cm}^{-3}$. Thermoelectric measurements show a moderately high Seebeck coefficient of $-72.6 \mu\text{V/K}$ at 640 K and a maximum power factor of $0.44 \times 10^{-3} \text{ W/m K}^2$ at 486 K. Demonstration of an ambient-stable semiconducting ErN thin film and its high thermoelectric power factor marks significant progress in rare-earth pnictide research and will help develop ErN-based spintronic and thermoelectric devices.

Published under license by AIP Publishing. <https://doi.org/10.1063/5.0041879>

Rare-earth nitrides (RENs) are an interesting family of materials with diverse electronic and magnetic properties but have remained relatively unexplored to date.^{1–4} RENs crystallize in the rock salt structure (B1) and exhibit localized strongly correlated 4f-electrons, which lead to their strong ferromagnetic properties useful for spin superlattices and spintronic applications.^{5–8} Solid-state alloys and heterostructures of RENs with conventional III-nitride semiconductors are promising for photonic applications in the infrared (IR) spectral range and for multi-wavelength optoelectronic devices.^{9–13} In addition, due to their 4f-intra-subshell transitions, RENs could be explored for single-photon emission and detection devices.^{5,14,15} ErN is a promising REN and exhibits a ferromagnetic ground state with a lattice constant of 4.85 Å in the bulk phase.¹⁶ Although there are only a handful of

experimental reports on ErN, almost all of them focus on bulk ErN growth.^{16–18} For example, in one of the earliest reports in the 1960s, a direct reaction of erbium with nitrogen inside an arc furnace and a synthesis of hydride followed by a reaction with ammonia were used to achieve dense specimens and fine powders of ErN, respectively.¹⁸ ErN obtained in both the methods was off-stoichiometric and contained nitrogen vacancies. Subsequent thermal evaporation of ErN on the quartz substrate and the transmission measurement yielded a bandgap of 2.4 eV.¹⁸ Similarly, more recently, physical vapor transport (PVT) has been used to grow ErN bulk crystals on tungsten foils at high temperatures (1620–1770 °C) in a pure nitrogen environment.¹⁶ Such ErN crystals were found to grow with (100) orientations with highly faceted planes and deviated from stoichiometry with the erbium

to nitrogen atomic ratio from 1.15 to 1.12.¹⁶ A minimum direct bandgap of 0.98 eV and two valence bands at the X-point separated by 0.37 eV were also subsequently deduced from photoemission measurements.¹⁷ Micron-sized ErN spheres have also found applications in Gifford–McMahon (GM) cryo-coolers that exhibited higher cooling power due to large specific heat of ErN at cryogenic temperatures.¹⁹

While experimental research on ErN has been scarce, several first-principles modeling studies have been performed to understand the electronic band structure and magnetic properties of ErN.^{20–22} Early spin-polarized local spin density approximation (LSDA) calculations showed ErN to be a nearly zero-gap semiconductor with the hole section of the Fermi surface close to the Γ -point and electron section near the X point of the Brillouin zone.^{21,23} However, as the conventional density functional theory underestimates the bandgap, exact knowledge of the gap energies remained unanswered. Hydrostatic pressure-dependent calculations also predicted an NaCl-type (B1) to CsCl-type (B2) structural phase transition in ErN at ~ 150 GPa with a stable ferromagnetic phase even at high temperatures.²⁴

Although research on ErN has remained at a nascent stage, Er-doped III-nitride semiconductors such as GaN,²⁵ InGaN,²⁶ and Er:YAG²⁷ have been studied extensively both experimentally and theoretically for their light-emission properties, electroluminescent devices,²⁸ solid-state lasers,²⁷ optical amplifiers,²⁹ and *p-i-n* diodes³⁰ in the optical communication window of $1.54\ \mu\text{m}$. The emission line at $1.54\ \mu\text{m}$ in Er-doped GaN originates from *4f*-intra-subshell transitions from trivalent Er^{+3} ions and is found to be robust with a very small thermal quenching.³¹ Despite all these developments, there are no reports on the thin film growth of ErN on single-crystalline substrates and studies on its microstructure and thermoelectric properties. RENs, in general, and ErN, in particular, however, could demonstrate high thermoelectric performance given the high mass of the rare-earth atoms, which is expected to result in low thermal conductivity in rare-earth pnictides, and semiconducting electronic nature with a high effective mass and low bandgap, which should result in a high thermoelectric power factor. Indeed, ErN's sister rare-earth scandium nitride (ScN) has already demonstrated a large thermoelectric power factor greater than $2.5 \times 10^{-3}\ \text{W/mK}^2$ in the temperature range of 500–600 K,^{32,33} which is higher than several well-known thermoelectric materials such as Bi_2Te_3 and PbTe .^{34–36} ScN is also currently explored for electronic devices with both *n*-type and *p*-type carrier transport. The thermal conductivity of ScN, however, is quite high 12–15 W/m K at 300 K, which results in its overall smaller thermoelectric figure of merit (ZT).^{33,37,38} Therefore, solid-solution alloys and heterostructures of ScN with ErN could help lower its thermal conductivity without decreasing high power factors.

Therefore, with the motivation of developing highly-efficient thermoelectric materials based on ErN and integrating ErN with semiconductors such as ScN, in this work, high-quality ErN thin films are deposited inside an ultrahigh vacuum (UHV) chamber and capped with AlN layers to stabilize in ambient conditions. ErN is found to exhibit a large thermoelectric power factor of $0.44 \times 10^{-3}\ \text{W/mK}^2$ at 450–550 K that is comparable with the power factor of well-known thermoelectric materials such as Bi_2Te_3 .^{39,40}

All films are deposited on MgO and Al_2O_3 substrates by dc-magnetron sputtering at a substrate temperature of 800°C and a base pressure of 2×10^{-9} Torr. Films are characterized by high-resolution thin film X-ray diffraction (HRXRD), high-resolution transmission

electron microscopy (HRTEM), Hall measurements, and thermoelectric characterization techniques [see the [supplementary material](#) (SM) for details]. To minimize oxidation, HRTEM sample preparation was performed with a focused ion beam (FIB) inside a high vacuum chamber followed by direct transfer and insertion into the TEM exposing the lamella for not more than 3 min to ambience.

As-deposited ErN thin films without any protective layer appear brownish-red in color [see Fig. 1(a)] and oxidize in ambient within ~ 20 –30 min after taking out of the UHV chamber. The brownish-red color of the ErN film is quite similar to that of ScN, indicating their resemblance in terms of their optical properties. Oxidation turns the film into a pinkish-white in color and eventually almost transparent [see Fig. 1(b)], which is also an indication of the higher bandgap of Er_2O_3 ($\sim 5.3\ \text{eV}$)^{41–43} with respect to that of ErN. It is important to note here that Er_2O_3 powder crystallizes in the cubic structure,⁴⁴ exhibits pink color,⁴⁵ and is attractive as a high-*k* dielectric material. The oxidation of the ErN thin film is consistent with previous research on bulk ErN that demonstrated ErN to be particularly reactive with moisture in the air that turns it into Er_2O_3 .^{16,18} In order to stabilize ErN thin films in ambience, 3 nm AlN was deposited *in situ* on top of ErN at the same growth temperature. The resultant ErN appeared slightly darker [see Fig. 1(c)] but was found to be ambient stable for at least 3 months [see Fig. 1(d)]. AlN is known for its oxidation resistance^{46–48} as it forms a thin Al_2O_3 layer on its surface that acts as an oxidation protective barrier. Limiting the thickness of AlN to 3 nm also ensures the measurement of ErN's electronic and thermoelectric properties (see the [supplementary material](#)).

Symmetric 2θ - ω HRXRD analysis reveals that AlN-coated ErN films grow with (002) and (111) orientations on (001) MgO and (0001) Al_2O_3 substrates. The (111) texture was found to be dominant for the film deposited on the (001) MgO substrate, while for the film

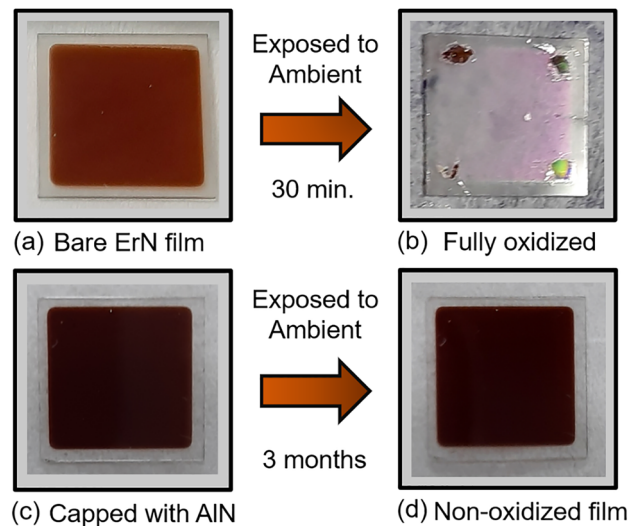


FIG. 1. (a) As-deposited (bare) ErN thin film without any protective layers demonstrating brownish-red color immediately after taking out from the UHV chamber. (b) Fully oxidized ErN film after 30 minutes of exposure to ambience. (c) ErN capped with a 3 nm AlN protective layer. (d) AlN-capped ErN layer is stable in ambience for at least 3 months.

deposited on the (0001) Al_2O_3 substrate, both textures exhibit similar peak intensities. For the film deposited on MgO [see Fig. 2(a)], the (111) and (002) film peaks appear at 31.8° and 36.9° , respectively, corresponding to a c -plane lattice constant of 4.87 \AA . Similarly, for the film deposited on the (0001) Al_2O_3 substrate [see Fig. 2(a)], the (111) and (002) peak appears at 31.8° and 36.8° , respectively, resulting in a c -plane lattice constant of 4.86 \AA . The lattice constant of ErN measured here is close to the previous report of 4.85 \AA for bulk ErN.¹⁶ The full-width-at-the-half-maxima (FWHM) of the rocking curve (ω -scan) corresponding to both the diffraction peaks on both the substrates are found to be greater than 3° , which represents their textured yet polycrystalline growth. The plan-view scanning electron microscopy (SEM) image of the film deposited on MgO substrates [Fig. 1(b)] shows triangular grains corresponding to the (111) orientations with grain sizes smaller than that on Al_2O_3 substrates [Fig. 1(c)].

High-angle annular dark-field scanning transmission electron microscopy (HAADF-STEM) images and electron diffraction pattern (EDP) are obtained to study the microstructure and crystallographic orientation of the ErN films with respect to the substrate. Low-magnification images [see Fig. 3(a)] show a sharp $\text{Al}_2\text{O}_3/\text{ErN}$ interface with large dark-field contrast at the interface arising from the difference in scattering angles of electrons interacting with the high atomic number Er and low atomic number Al, respectively. The film appears to grow coherently for the first $\sim 30\text{--}50 \text{ nm}$, maintaining a local epitaxial relationship with the substrate. However, the epitaxy breaks after $\sim 30\text{--}50 \text{ nm}$ of growth, and columnar grains appear with an average width of $\sim 40\text{--}50 \text{ nm}$. The surface features on the plan-view SEM image are, therefore, the top of such columns with a pyramidal shape. Along with the broken epitaxy, the grains are rotated along the in-plane directions and V-shaped structural defects appear. Such

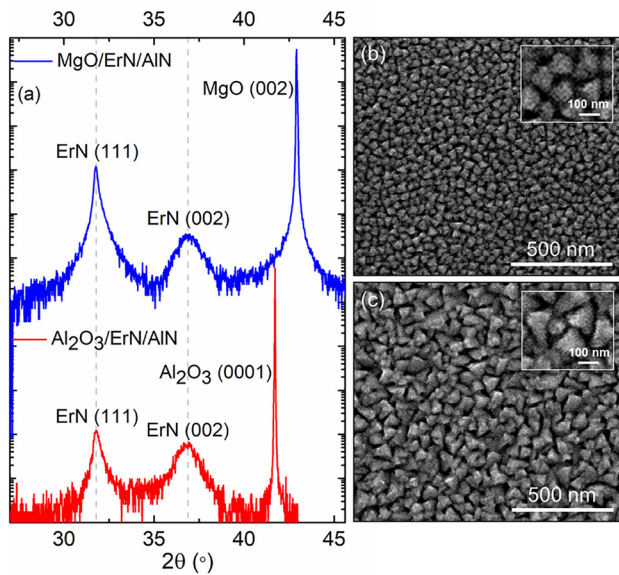


FIG. 2. (a) Symmetric 2θ - ω HRXRD pattern of the ErN thin film deposited on (001) MgO and (0001) Al_2O_3 substrates showing (002) and (111) oriented growth. The relative intensity of (111) texture with respect to the (002) is larger for films deposited on MgO substrates. Plan-view SEM images of (b) MgO/ErN and (c) $\text{Al}_2\text{O}_3/\text{ErN}$ are presented that exhibit mostly triangular grains.

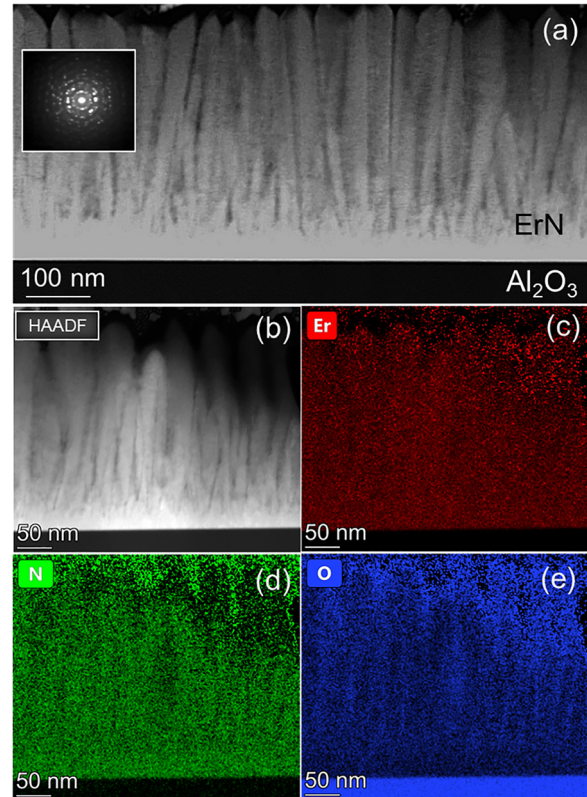


FIG. 3. (a) HAADF-STEM micrograph of the ErN film deposited on the Al_2O_3 substrate showing columnar grain growth after $\sim 30\text{--}50 \text{ nm}$ of smooth film deposition with a flat interface. V-shaped structural defects can be seen as a result of the growth temperature. (b) highlights the V-shaped defects. (c) Er (d) N and (e) O TEM-EDS maps are presented, which exhibit a sharp ErN/ Al_2O_3 interface and uniform Er as well as N distribution.

V-shaped defects are quite common for nitride thin films such as ScN, TiN, and GaN⁴⁹⁻⁵¹ and appear primarily due to the Ehrlich-Schwoebel (E-S) barrier in a lateral direction that cannot be overcome due to lower adatom mobility for intra-grain migration.⁴⁹ The V-shaped defects are structural voids [Fig. 3(b)], which are depleted of Er and N [Figs. 3(c) and 3(d)], but rich with O [Fig. 3(e)]. The selective area EDP collected from the film [see Fig. 3(a) inset] show rings with bright spots that represent textured polycrystalline growth. STEM energy-dispersive x-ray spectroscopy (EDS) analysis also shows that the Er and N content is uniform throughout the film and a sharp interface with the Al_2O_3 substrate. The film also contains a higher oxygen concentration close to the surface regions as compared to the region at the film-substrate interface. However, it is not possible to distinguish the amount of oxidation occurring from the growth and from the few minutes of transport to the instrument at ambient after HRTEM sample preparation.

High-magnification HAADF-STEM images (see Fig. 4) show atomic fringes corresponding to ErN grains with the electron beam along [100] [Fig. 4(a)] and [110] [Fig. 4(b)] with the c -axis [001] pointing along the growth direction on the (0001) Al_2O_3 substrate. The substrate layer appears dark due to the high dark-field contrast with the

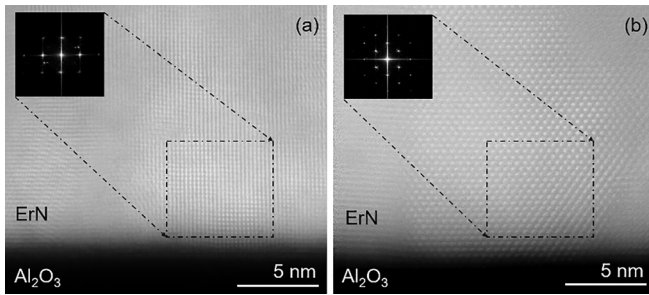


FIG. 4. High-magnification HAADF-STEM micrograph of the ErN–Al₂O₃ interface and FFT in the inset showing ErN grains along the (a) [100] and (b) [110] directions with [001] along the film growth direction.

ErN layer. Small (002) grains in the zone-axis, as well as out-of-zone-axis grains with diameters of 5–20 nm, are seen in Fig. 4(a). The interplanar spacing measured between the (002) lattice planes confirms the lattice constant of ErN. Fast Fourier Transform (FFT) from the selected region also shows the cubic diffraction pattern corresponding to the (002) grain growth and is indexed in the SM. A large grain that is rotated by 45° with respect to the incident beam [100] direction with the *c*-axis [001] along the growth direction is shown in Fig. 4(b), and analysis of its FFT with angles of ~70°, ~55°, and ~55° between the lower order spots identifies the incident beam direction to be along [110].

Room-temperature electronic properties of the ErN films deposited on MgO and Al₂O₃ substrates are measured using the Hall method and exhibit resistivities of 4.3 mΩ–cm and 6.4 mΩ–cm respectively. Similarly, room-temperature mobilities of 3.4 cm²/V s and 0.6 cm²/V s and carrier concentrations of 4.3 × 10²⁰ cm⁻³ and 1.4 × 10²¹ cm⁻³ were measured for both the films, respectively. The measured resistivity of ErN represents its degenerate semiconducting nature and is about an order of magnitude higher than that of ScN. It is interesting to note that bulk ErN described in the 1960s exhibited a much lower resistivity of 7.9 × 10⁻⁵ Ω cm possibly due to higher defect concentrations.¹⁸ The high carrier concentration of ErN is presumed to be due to the presence of defects including oxygen impurities arising from target contamination and nitrogen vacancies. It is important to note that several emerging nitrides such as ScN³³ and Zn₃N₂⁵² also exhibit degenerate semiconducting electronic nature and have attracted significant attention in recent years for several potential applications. Such a large carrier density also reduces the mobility of ErN films due to increased electron-electron scattering. In order to ascertain that the capping layer does not influence the Hall, electronic, and Seebeck measurements, separate ErN films were deposited on MgO substrates with a 3 nm TiN capping layer instead of AlN at the ErN deposition conditions, which show almost the same resistivity, mobility, carrier concentrations, and Seebeck coefficient.

Room-temperature optical properties such as absorption spectrum, bandgap, and photoluminescence (PL) of the ErN films are measured to gain insight into its electronic structure. ErN exhibits (see the [supplementary material](#), Fig. S2) high absorbance in the range of (2–6) × 10⁷ cm⁻¹, which results from its large carrier concentration and the presence of defects. Such high absorbance would limit light absorption close to the ErN surface. The Tauc plot as a function of the photon energy demonstrates a clear absorption edge, and a bandgap of 1.88–1.92 eV is measured for ErN deposited on both substrates. The

measured bandgap of ErN is smaller than the previously measured gap of 2.4 eV on evaporated ErN from bulk on quartz substrates¹⁸ and is close to the bandgap of ScN (2.2 eV). No clear sub-bandgap absorption was noticed from the absorption spectrum. Photoluminescence (PL) measurements performed with variable laser excitation wavelengths of 325, 340, 405, and 510 nm at room temperature yield no clear ErN peaks either in the visible (300 nm–800 nm) or in the near IR (800 nm–2000 nm), indicating that as predicted by the modeling, ErN is likely to be an indirect bandgap semiconductor. Detailed photoemission and modeling work in this regard will be reported subsequently.

In order to understand ErN's potential for thermoelectric applications, the Seebeck coefficient and electrical conductivity of the films are measured from 334 K to 640 K with AlN and TiN capping layers, respectively, [see Fig. 5(a) and 5(b)]. The maximum measurement temperature was limited to less than 650 K in order to prevent possibilities for oxidation. At 334 K, AlN and TiN capped ErN exhibit moderate Seebeck coefficients of -45.5 μV/K and -42.4 μV/K, respectively. With an increase in temperature, the Seebeck coefficient increases monotonically and exhibited maxima of -72.6 μV/K and -66.5 μV/K at 640 K, respectively, for both the films. In line with the increase in the Seebeck coefficient, the electrical conductivity was found to decrease from 144.9 Scm⁻¹ at 334 K to 56.3 Scm⁻¹ at 640 K. Such a small decrease in electrical conductivity is representative of ErN's degenerate semiconducting nature with large carrier concentrations. It is quite interesting that the Seebeck coefficient of the ErN thin film near room temperature is quite similar to the Seebeck coefficient of -36 μV/K measured on bulk ErN in the 1960s.¹⁸ Although the measured Seebeck coefficient of ErN is significantly smaller than that of ScN,³⁵ both the materials show almost twice an increase in the Seebeck coefficient with an increase in temperature from 334 K to 640 K. The relatively smaller overall Seebeck coefficient of ErN is a result of its high carrier concentration. However, it is also interesting to note that until about eight years ago and before the development of high-quality ScN thin films with a reduced carrier concentration and high mobility, ScN is also used to show smaller Seebeck coefficients and higher electrical conductivity.¹⁸ Therefore, further progress in epitaxial growth methods and controlling defect density could yield higher thermoelectric properties in ErN films (Fig. 5).

With the measured Seebeck coefficient and electrical conductivity, the thermoelectric power factor of ErN is determined as a function of temperature [see Fig. 5(c)]. The power factor exhibits an increase from 334 K to 446 K, followed by saturation from 446 K to 486 K and a subsequent decrease. A maximum power factor of 0.44 × 10⁻³ W/m K² at 486 K was achieved for ErN with the AlN capping layer. The power factors are slightly smaller for the films capped with a TiN layer. Although the measured power factor of ErN is smaller than that of ScN in the same temperature range, it is comparable to the power factor of well-known thermoelectric material Bi₂Te₃, PbTe, etc.^{39,40,53} In spite of its lower power factor, the overall thermoelectric figure of merit (ZT) of ErN could be higher given its expected low thermal conductivity.

In conclusion, a high thermoelectric power factor of 0.44 × 10⁻³ W/m K² at 486 K is achieved in rare-earth semiconducting ErN thin films deposited inside an ultra-high vacuum chamber by magnetron sputtering. As-deposited ErN is found to be prone to oxidation. A 3 nm thin AlN capping layer deposited *in situ* on top of ErN at the

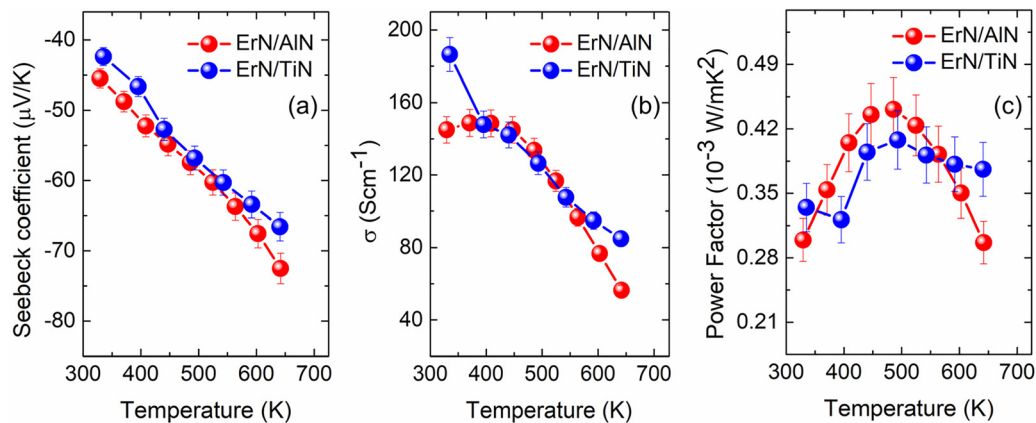


FIG. 5. (a) Seebeck coefficient, (b) electrical conductivity, and (c) thermoelectric power factor of the ErN thin film capped with oxidation-resistant AlN and TiN layers and deposited on Al_2O_3 substrates are presented. The Seebeck coefficient is found to increase with the increase in temperature, while the electrical conductivity decreases slightly representing ErN's degenerate semiconducting nature. A maximum thermoelectric power factor of $0.44 \times 10^{-3} \text{ W/mK}^2$ at 486 K was achieved.

growth temperature was found to prevent oxidation and make it ambient stable for at least 3 months. ErN films are found to grow with (002) and (111) orientations and exhibit textured polycrystalline growth. HR(S)/TEM imaging revealed abrupt and sharp ErN/substrate interfaces and columnar growth. Degenerate semiconducting behavior was achieved in ErN films with a high carrier concentration ($1.4 \times 10^{21} \text{ cm}^{-3}$) and low mobility due to the presence of defects and impurities. In addition, a direct bandgap optical transition at 1.88–1.92 eV was measured. The development of an ambient stable high-quality ErN thin film and demonstration of its high thermoelectric power factor will attract rare-earth nitrides for designing highly efficient thermoelectric and optoelectronic devices.

See the [supplementary material](#) for information related to the growth process, HRXRD and HRTEM characterization, HRTEM sample preparation, optical properties of ErN films, details on electrical and thermoelectric characterization, and on the choice of the capping layers, and their thicknesses and possible impacts on the electrical and thermoelectric characterization.

K.U. and B.S. acknowledge support from the International Centre for Materials Science (ICMS) and the Sheikh Saqr Laboratory (SSL) of the Jawaharlal Nehru Centre for Advanced Scientific Research (JNCASR). BS acknowledges the Young Scientist Research Award (YSRA) from the Board of Research in Nuclear Sciences (BRNS), Department of Atomic Energy (DAE), India, with Grant No. 59/20/10/2020-BRNS/59020 for financial support. K.U. acknowledges Shashidhara Acharya, Bidesh Biswas, Dheemahi Rao, and Krishna Chand Maurya for assistance in experimental work. The authors acknowledge the facilities of Sydney Microscopy and Microanalysis at The University of Sydney.

DATA AVAILABILITY

The data that support the findings of this study are available from the corresponding author upon reasonable request.

REFERENCES

- C.-G. Duan, R. F. Sabirianov, W. N. Mei, P. A. Dowben, S. S. Jaswal, and E. Y. Tsymlal, *J. Phys. Condens. Matter* **19**, 315220 (2007).
- F. Natali, N. O. V. Plank, J. Galipaud, B. J. Ruck, H. J. Trodahl, F. Semond, S. Sorieul, and L. Hirsch, *J. Cryst. Growth* **312**, 3583 (2010).
- Z. Altounian, X. Chen, L. X. Liao, D. H. Ryan, and J. O. Ström-Olsen, *J. Appl. Phys.* **73**, 6017 (1993).
- C. M. Aerts, P. Strange, M. Horne, W. M. Temmerman, Z. Szotek, and A. Svane, *Phys. Rev. B* **69**, 045115 (2004).
- F. Natali, B. J. Ruck, N. O. V. Plank, H. J. Trodahl, S. Granville, C. Meyer, and W. R. L. Lambrecht, *Prog. Mater. Sci.* **58**, 1316 (2013).
- N. O. V. Plank, F. Natali, J. Galipaud, J. H. Richter, M. Simpson, H. J. Trodahl, and B. J. Ruck, *Appl. Phys. Lett.* **98**, 112503 (2011).
- P. Wachter, *Adv. Mater. Phys. Chem.* **05**, 96 (2015).
- K. Senapati, M. G. Blamire, and Z. H. Barber, *Nat. Mater.* **10**, 849 (2011).
- Z. Y. Sun, Y. Q. Yan, T. B. Smith, W. P. Zhao, J. Li, J. Y. Lin, and H. X. Jiang, *Appl. Phys. Lett.* **114**, 222105 (2019).
- Z. Y. Sun, H. L. Gong, Y. Q. Yan, T. B. Smith, J. Li, J. Y. Lin, and H. X. Jiang, *J. Appl. Phys.* **127**, 243107 (2020).
- P. C. de Sousa Filho, J. F. Lima, and O. A. Serra, *J. Braz. Chem. Soc.* **26**, 2471 (2015).
- J. M. Zavada, N. Nepal, C. Ugolini, J. Y. Lin, H. X. Jiang, R. Davies, J. Hite, C. R. Abernathy, S. J. Pearton, E. E. Brown, and U. Hömmerich, *Appl. Phys. Lett.* **91**, 054106 (2007).
- K. P. O'Donnell and B. Hourahine, *Eur. Phys. J. Appl. Phys.* **36**, 91 (2006).
- R. Kolesov, K. Xia, R. Reuter, R. Stöhr, A. Zappe, J. Meijer, P. R. Hemmer, and J. Wrachtrup, *Nat. Commun.* **3**, 1029 (2012).
- T. Zhong, J. M. Kindem, J. G. Bartholomew, J. Rochman, I. Craiciu, V. Verma, S. W. Nam, F. Marsili, M. D. Shaw, A. D. Beyer, and A. Faraon, *Phys. Rev. Lett.* **121**, 183603 (2018).
- H. A. Al Atabi, Z. F. Al Auda, B. Padavala, M. Craig, K. Hohn, and J. H. Edgar, *Cryst. Growth Des.* **18**, 3762 (2018).
- M. A. McKay, Q. W. Wang, H. A. Al-Atabi, Y. Q. Yan, J. Li, J. H. Edgar, J. Y. Lin, and H. X. Jiang, *Appl. Phys. Lett.* **116**, 171104 (2020).
- N. Sclar, *J. Appl. Phys.* **35**, 1534 (1964).
- T. Nakano, S. Masuyama, Y. Hirayama, T. Izawa, T. Nakagawa, Y. Fujimoto, T. Irie, E. Nakamura, and T. A. Yamamoto, *Appl. Phys. Lett.* **101**, 251908 (2012).
- A. G. Petukhov, W. R. L. Lambrecht, and B. Segall, *Phys. Rev. B* **53**, 4324 (1996).

- ²¹P. Larson, W. R. L. Lambrecht, A. Chantis, and M. van Schilfgaarde, *Phys. Rev. B* **75**, 045114 (2007).
- ²²S. Dergal, A. E. Merad, and B. N. Brahma, *Am. J. Mater. Sci. Technol.* **2**, 40 (2013).
- ²³A. G. Petukhov, W. R. L. Lambrecht, and B. Segall, *MRS Proc.* **337**, 583 (1994).
- ²⁴P. Pandit, V. Srivastava, M. Rajagopalan, and S. P. Sanyal, *Physica B* **405**, 2245 (2010).
- ²⁵V. X. Ho, Y. Wang, B. Ryan, L. Patrick, H. X. Jiang, J. Y. Lin, and N. Q. Vinh, *J. Lumin.* **221**, 117090 (2020).
- ²⁶A. Sedhain, C. Ugolini, J. Y. Lin, H. X. Jiang, and J. M. Zavada, *Appl. Phys. Lett.* **95**, 041113 (2009).
- ²⁷N. Ter-Gabrielyan, V. Fromzel, X. Mu, H. Meissner, and M. Dubinskii, *Opt. Lett.* **38**, 2431 (2013).
- ²⁸A. J. Steckl, J. C. Heikenfeld, L. Dong-Seon, M. J. Garter, C. C. Baker, Y. Wang, and R. Jones, *IEEE J. Sel. Top. Quantum Electron.* **8**, 749 (2002).
- ²⁹R. Dahal, C. Ugolini, J. Y. Lin, H. X. Jiang, and J. M. Zavada, *Appl. Phys. Lett.* **95**, 111109 (2009).
- ³⁰R. Dahal, C. Ugolini, J. Y. Lin, H. X. Jiang, and J. M. Zavada, *Appl. Phys. Lett.* **97**, 141109 (2010).
- ³¹D. K. George, M. D. Hawkins, M. McLaren, H. X. Jiang, J. Y. Lin, J. M. Zavada, and N. Q. Vinh, *Appl. Phys. Lett.* **107**, 171105 (2015).
- ³²S. Kerdsonpanya, N. Van Nong, N. Pryds, A. Žukauskaitė, J. Jensen, J. Birch, J. Lu, L. Hultman, G. Wingqvist, and P. Eklund, *Appl. Phys. Lett.* **99**, 232113 (2011).
- ³³P. V. Burmistrova, J. Maassen, T. Favaloro, B. Saha, S. Salamat, Y. Rui Koh, M. S. Lundstrom, A. Shakouri, and T. D. Sands, *J. Appl. Phys.* **113**, 153704 (2013).
- ³⁴P. Eklund, S. Kerdsonpanya, and B. Alling, *J. Mater. Chem. C* **4**, 3905 (2016).
- ³⁵D. Rao, B. Biswas, E. Flores, A. Chatterjee, M. Garbrecht, Y. R. Koh, V. Bhatia, A. I. K. Pillai, P. E. Hopkins, M. Martin-Gonzalez, and B. Saha, *Appl. Phys. Lett.* **116**, 152103 (2020).
- ³⁶B. Biswas and B. Saha, *Phys. Rev. Mater.* **3**, 020301 (2019).
- ³⁷B. Saha, J. A. Perez-Taborda, J. H. Bahk, Y. R. Koh, A. Shakouri, M. Martin-Gonzalez, and T. D. Sands, *Phys. Rev. B* **97**, 085301 (2018).
- ³⁸S. Kerdsonpanya, O. Hellman, B. Sun, Y. K. Koh, J. Lu, N. Van Nong, S. I. Simak, B. Alling, and P. Eklund, *Phys. Rev. B* **96**, 195417 (2017).
- ³⁹F. F. Oktavianoni, K. Singsoog, and M. S. Muntini, *J. Phys. Conf. Ser.* **1428**, 012007 (2020).
- ⁴⁰B. Zhang, J. Sun, H. E. Katz, F. Fang, and R. L. Opila, *ACS Appl. Mater. Interfaces* **2**, 3170 (2010).
- ⁴¹G. Adachi and N. Imanaka, *Chem. Rev.* **98**, 1479 (1998).
- ⁴²C. H. Kao, H. Chen, Y. T. Pan, J. S. Chiu, and T. C. Lu, *Solid State Commun.* **152**, 504 (2012).
- ⁴³H. S. Kamineni, V. K. Kamineni, R. L. Moore, S. Gallis, A. C. Diebold, M. Huang, and A. E. Kaloyeros, *J. Appl. Phys.* **111**, 013104 (2012).
- ⁴⁴M. P. Singh, C. S. Thakur, K. Shalini, N. Bhat, and S. A. Shivashankar, *Appl. Phys. Lett.* **83**, 2889 (2003).
- ⁴⁵E. Staritzky, *Anal. Chem.* **28**, 2023 (1956).
- ⁴⁶S. Cwik, S. M. J. Beer, S. Hoffmann, M. Krasnopolski, D. Rogalla, H.-W. Becker, D. Peeters, A. Ney, and A. Devi, *ACS Appl. Mater. Interfaces* **9**, 27036 (2017).
- ⁴⁷R. Vidyasagar, S. Kitayama, H. Yoshitomi, T. Kita, T. Sakurai, and H. Ohta, *Eur. Phys. J. B* **86**, 52 (2013).
- ⁴⁸J. Kennedy, S. Granville, A. Markwitz, B. J. Ruck, and H. J. Trodahl, *Nucl. Instrum. Methods Phys. Res., Sect. B* **266**, 1558 (2008).
- ⁴⁹D. Rao, B. Biswas, S. Acharya, V. Bhatia, A. I. K. Pillai, M. Garbrecht, and B. Saha, *Appl. Phys. Lett.* **117**, 212101 (2020).
- ⁵⁰J. Smalc-Koziorowska, E. Grzanka, R. Czernecki, D. Schiavon, and M. Leszczyński, *Appl. Phys. Lett.* **106**, 101905 (2015).
- ⁵¹J. Gao, J. Zhang, X. Zhu, X. Wu, C. Mo, S. Pan, J.-L. Liu, and F.-Y. Jiang, *J. Appl. Crystallogr.* **52**, 637 (2019).
- ⁵²Y. Wang, T. Ohsawa, Y. Kumagai, K. Harada, F. Oba, and N. Ohashi, *Appl. Phys. Lett.* **115**, 092104 (2019).
- ⁵³V. Sharma, M. Saxena, and G. S. Okram, *AIP Conf. Proc.* **2100**, 020081 (2019).